THE PLANETARY SCIENCE JOURNAL, 4:97 (20pp), 2023 May https://doi.org/10.3847/PSJ/acd32f

Depletion of ^{13}C in CO in the Atmosphere of Mars Suggested by ExoMars-TGO/NOMAD Observations

S. Aoki[1,2], K. Shiobara[3], N. Yoshida[3], L. Trompet[2], T. Yoshida[3], N. Terada[3], H. Nakagawa[3], G. Liuzzi[4], A. C. Vandaele[2], I. R. Thomas[2], G. L. Villanueva[5], M. A. Lopez-Valverde[6], A. Brines[6], M. R. Patel[7], S. Faggi[5,8], F. Daerden[2], J. T. Erwin[2], B. Ristic[2], G. Bellucci[9], J. J. Lopez-Moreno[6], H. Kurokawa[10,11], and Y. Ueno[11]

[1] Department of Complexity Science and Engineering, Graduate School of Frontier Sciences, The University of Tokyo, 5-1-5 Kashiwanoha, Kashiwa, Chiba 277-8561, Japan; shohei.aoki@edu.k.u-tokyo.ac.jp

[2] Royal Belgian Institute for Space Aeronomy, 3 Avenue Circulaire, B-1180 Brussels, Belgium

[3] Tohoku University, 6-3, Aramaki Aza-Aoba, Sendai 980-8578, Japan

[4] Scuola di Ingegneria, Universitá degli Studi della Basilicata, Via dell'Ateneo Lucano, 10, I-85100 Potenza, Italy

[5] NASA Goddard Space Flight Center, 8800 Greenbelt Road, Greenbelt, 20771 MD, USA

[6] Instituto de Astrofísica de Andalucía, Glorieta de la Astronomia, E-18008 Granada, Spain

[7] School of Physical Sciences, The Open University, Milton Keynes, MK7 6AA, UK

[8] American University, 4400 Massachusetts Avenue Northwest, Washington, DC 20016, USA

[9] Istituto Nazionale di Astrofisica, Via del Fosso del Cavaliere 100, I-00133 Rome, Italy

[10] Department of Earth Science and Astronomy, Graduate School of Arts and Sciences, The University of Tokyo, Japan

[11] Tokyo Institute of Technology, 2-12-1 Ookayama, Tokyo 152-8550, Japan

Received 2022 December 22; revised 2023 May 2; accepted 2023 May 4; published 2023 May 26

Abstract

The atmosphere of Mars is mainly composed by carbon dioxide (CO_2). It has been predicted that photodissociation of CO_2 depletes ^{13}C in carbon monoxide (CO). We present the carbon $^{13}C/^{12}C$ isotopic ratio in CO at 30–50 km altitude from the analysis of the solar occultation measurements taken by the instrument Nadir and Occultation for Mars Discovery on board the ExoMars Trace Gas Orbiter (ExoMars-TGO). We retrieve $^{12}C^{16}O$, $^{13}C^{16}O$, and $^{12}C^{18}O$ volume mixing ratios from the spectra taken at 4112–4213 cm^{-1}, where multiple CO isotope lines with similar intensities are available. The intensities of the $^{12}C^{16}O$ lines in this spectral range are particularly sensitive to temperature, thus we derive the atmospheric temperature by retrieving CO_2 density with simultaneously measured spectra at 2966–2990 cm^{-1}. The mean $\delta\ ^{13}C$ value obtained from the $^{13}C^{16}O/^{12}C^{16}O$ ratios is −263‰, and the standard deviation and standard error of the mean are 132‰ and 4‰, respectively. The relatively large standard deviation is due to the strong temperature dependences in the $^{12}C^{16}O$ lines. We also examine the $^{13}C^{16}O/^{12}C^{18}O$ ratio, whose lines are less sensitive to temperature. The mean δ value obtained with $^{12}C^{18}O$ instead of $^{12}C^{16}O$ is −82‰ with smaller standard deviation, 60‰. These results suggest that CO is depleted in ^{13}C when compared to CO_2 in the Martian atmosphere as measured by the Curiosity rover. This depletion of ^{13}C in CO is consistent with the CO_2 photolysis-induced fractionation, which might support a CO-based photochemical origin of organics in Martian sediments.

Unified Astronomy Thesaurus concepts: Planetary atmospheres (1244)

1. Introduction

Isotopic ratios in trace gases are sensitive to short-term process (∼days/years), such as photochemistry, sublimation-condensation, diffusion, as well as for long-term effects (∼million/billion years), such as degassing and escaping to space (e.g., Lammer et al. 2020). The current atmosphere of Mars is mainly composed by carbon dioxide (CO_2, ∼96%). Atmospheric CO_2 can be photodissociated with ultraviolet light, but the CO_2-rich atmosphere is maintained by the reaction between CO and OH to reproduce CO_2 ($CO + OH \rightarrow CO_2 + H$). Schmidt et al. (2013) showed with quantum mechanical calculations that the UV absorption cross-section of $^{13}CO_2$ is several tenths of a percent less than that of $^{12}CO_2$, which suggests that faster photolysis of $^{12}CO_2$ with respect to $^{13}CO_2$ could induce an isotopic depletion of ^{13}C relative to ^{12}C in CO, $\delta\ ^{13}C$ (see definition below) by about −200‰ relative to initial CO. With calculation by a one-dimensional photochemical model considering the isotopic fractionation, Yoshida et al. (2023) have predicted that CO can be depleted in ^{13}C compared with CO_2 by about −170‰ in the lower atmosphere (below 50 km) via photolysis of CO_2. A similar depletion of ^{13}C in CO that is probably due to photolysis-induced fractionation has in fact been observed in Earth's mesosphere (Beale et al. 2016).

Recently, from the measurements made by Curiosity rover, House et al. (2022) showed that ∼3.5 billion years old sedimentary organic carbon at Gale crater on Mars is depleted in ^{13}C down to about −137‰ relative to the Vienna Pee Dee Belemnite (V-PDB). The $\delta\ ^{13}C$ [‰] value is defined by $(R/R_s - 1) \times 1000$, where the reference value of the V-PDB for the $^{13}C/^{12}C$ ratio (R_s) is 1.123×10^{-2}. One possible explanation for this is that it is due to the photochemical production and deposition of organic materials via CO fractionated through the photolysis of CO_2, which suggests that the early-Martian organics were originated from CO in the early Mars atmosphere (Lammer et al. 2020). Thus, knowledge of the carbon isotopic ratio in CO is essential for understanding the origin of the organic compounds on Mars.

However, there are no accurate measurements of $^{13}C/^{12}C$ in CO available in the literature and previous observations of carbon isotopic ratio in the Martian atmosphere are limited to

CO_2. Webster et al. (2013) showed that the $^{13}C/^{12}C$ in CO_2 is enriched in ^{13}C, 46 ± 4‰ with respect to V-PDB from the measurements with Tunable Laser Spectrometer on board the Curiosity rover operating over the Gale Crater. Recent solar occultation measurements have not shown significant variability of this latter ratio over locations and seasons below 50 km (Liuzzi et al. 2022). Lellouch et al. (1989) suggested the $^{13}C/^{12}C$ ratio in CO is not compatible with the terrestrial value by telescope observations in the millimeter spectral ranges. However, these results strongly depend on the thermal profiles assumed in the radiative transfer calculation. Moreover, Clancy & Muhleman (1990) pointed out that the radiative transfer calculation performed in Lellouch et al. (1989) are incorrect.

The ExoMars Trace Gas Orbiter (TGO) has two high spectral resolution spectrometers—Nadir and Occultation for Mars Discovery (NOMAD; Vandaele et al. 2018) and Atmospheric Chemistry Suite (ACS; Korablev et al. 2018)—that carry out solar occultation measurements, which allows us to perform sensitive measurements of trace gases on Mars. Characterizing the isotopic ratios in trace gases is one of their main science goals. In fact, previous studies with TGO measurements have revealed the isotopic ratios of carbon and oxygen in CO_2 from 70 to 100 km, hydrogen and oxygen in water vapor from surface to 50 km, and chlorine in HCl in the lower atmosphere (Alday et al. 2019, 2021a, 2021b; Vandaele et al. 2019; Liuzzi et al. 2021; Trokhimovskiy et al. 2021; Villanueva et al. 2021, 2022). In this study, we investigate the carbon isotopic ratio in CO from the NOMAD data set taken between 2022 March and April. We perform the analysis by simultaneously fitting the spectra taken at four different diffraction orders to reduce the uncertainty in the obtained isotopic ratio. The details of the data set and analysis are described in Section 2, and the observational results are shown and discussed in Section 3.

2. Data Set and Analysis

NOMAD is a spectrometer on board ExoMars TGO that has three spectral channels: a Solar Occultation (SO) channel operating at 2.3–4.3 μm, a Limb Nadir and solar Occultation (LNO) channel at 2.3–3.8 μm, and an Ultraviolet and Visible Spectrometer (UVIS) channel at 200–650 nm (Vandaele et al. 2018). In this study, the solar occultation measurements taken by the SO channel are analyzed. One of the advantages of the NOMAD SO channel when compared to the near-infrared spectrometers on board previous missions is its relatively high spectral resolution ($\lambda/d\lambda \sim 17{,}000$ for the SO channel), which is achieved by an echelle grating. The selection of the grating diffraction orders is performed by the Acousto Optical Tunable Filter (AOTF). Because the order selection by the AOTF is instantaneous, the SO channel can measure five or six different diffraction orders in ∼1 s, which provides a vertical sampling step of less than ∼1 km. Another advantage of NOMAD is its high signal-to-noise ratio (greater than 1000) thanks to the solar occultation technique, which allows us to perform sensitive searches of absorption features from the trace gases and measurements of their isotopic ratios.

The spectra measured through the Mars atmosphere are divided by the reference solar spectrum to obtain transmittances. This division removes systematic instrumental effects. The reference solar spectrum is created by extrapolation of those recorded above the atmosphere (see Trompet et al. 2022a for details). The calculated transmittances are compared with synthetic spectra computed by a radiative transfer model to retrieve abundances of trace gases and aerosols along the line of sight (see below for further details). To properly model the spectra measured by the NOMAD SO channel, a good knowledge of the instrumental line shape (ILS) function and the AOTF transfer function is required. These instrumental functions have been accurately characterized by in-flight calibration measurements (see Villanueva et al. 2022 for details) and implemented in the radiative transfer calculations.

Figure 1 shows the synthetic spectra for the NOMAD SO observations with diffraction orders 186 (4180–4213 cm^{-1}), 185 (4157–4190 cm^{-1}), 184 (4134–4167 cm^{-1}), and 183 (4112–4145 cm^{-1}), which demonstrates that $^{12}C^{16}O$, $^{13}C^{16}O$, and $^{12}C^{18}O$ lines should be clearly visible in these spectral ranges. The intensities of these lines as seen in the NOMAD spectra are comparable, so that similar weighting functions along the line of sight are ensured. However, there are some challenges when working on the spectra taken in these diffraction orders. The first challenge is the fact that many weak features due to CO lines coming from adjacent diffraction orders appear in the spectra (see the NOMAD synthetic spectra that separately illustrate the contributions of the main and adjacent orders, shown in Figure A1), due to the nature of the AOTF transfer function (Villanueva et al. 2022). The second challenge is that the intensities of the $^{12}C^{16}O$ lines are highly sensitive to temperature. The lower-state energy of the transition E'' parameter for the main $^{12}C^{16}O$ lines is greater than 1000 cm^{-1} (see the E'' parameters of CO lines in diffraction orders 183–186, shown in Figure A2). Thus, a good knowledge of the AOTF transfer function and the temperature at the time and place of the observation is required. Villanueva et al. (2022) performed an in-depth investigation of the AOTF transfer function based on the in-flight calibration measurements of the Sun, which allows us to improve the quality of the molecular retrievals. We constrain the temperature by retrieving it from simultaneous measurement of the CO_2 band in diffraction order 132 (2966–2990 cm^{-1}). The errors in the retrieved isotopic ratio due to the uncertainties in the AOTF transfer function and temperature used in the radiative transfer calculation are also evaluated.

The observations with the diffraction orders 185, 184, and 183 have been added to the nominal operation of the NOMAD SO channel in 2022 March. In this study, we analyzed eight orbits taken between 2022 March and April, which simultaneously measure orders 183, 184, 185, 186, and 132. Table 1 shows the geometry information of these orbits. The measurements are performed in the northern fall season (Ls = 182°–205°) over the middle and high latitudes, except for the last orbit measured on 2022 April 8 that was acquired over the equatorial region.

The retrieval of both temperature and CO abundances is conducted by Atmospheric Spectra Inversion Modular Utility Tools (ASIMUT)—Asimut Lidort VLidort (ALVL) radiative transfer and inversion code (Vandaele et al. 2006). The temperature profiles are derived from CO_2 density profiles using the hydrostatic equilibrium equation. The CO_2 density profiles are retrieved from the measurements at diffraction orders 132 (2966–2990 cm^{-1}), which is suitable to scan the troposphere (0–50 km). The method is described in detail in Trompet et al. (2022a). The baseline level of the spectra is gradually decreased toward the lower altitude, due to a high density of aerosols along the line of sight. In this study, no

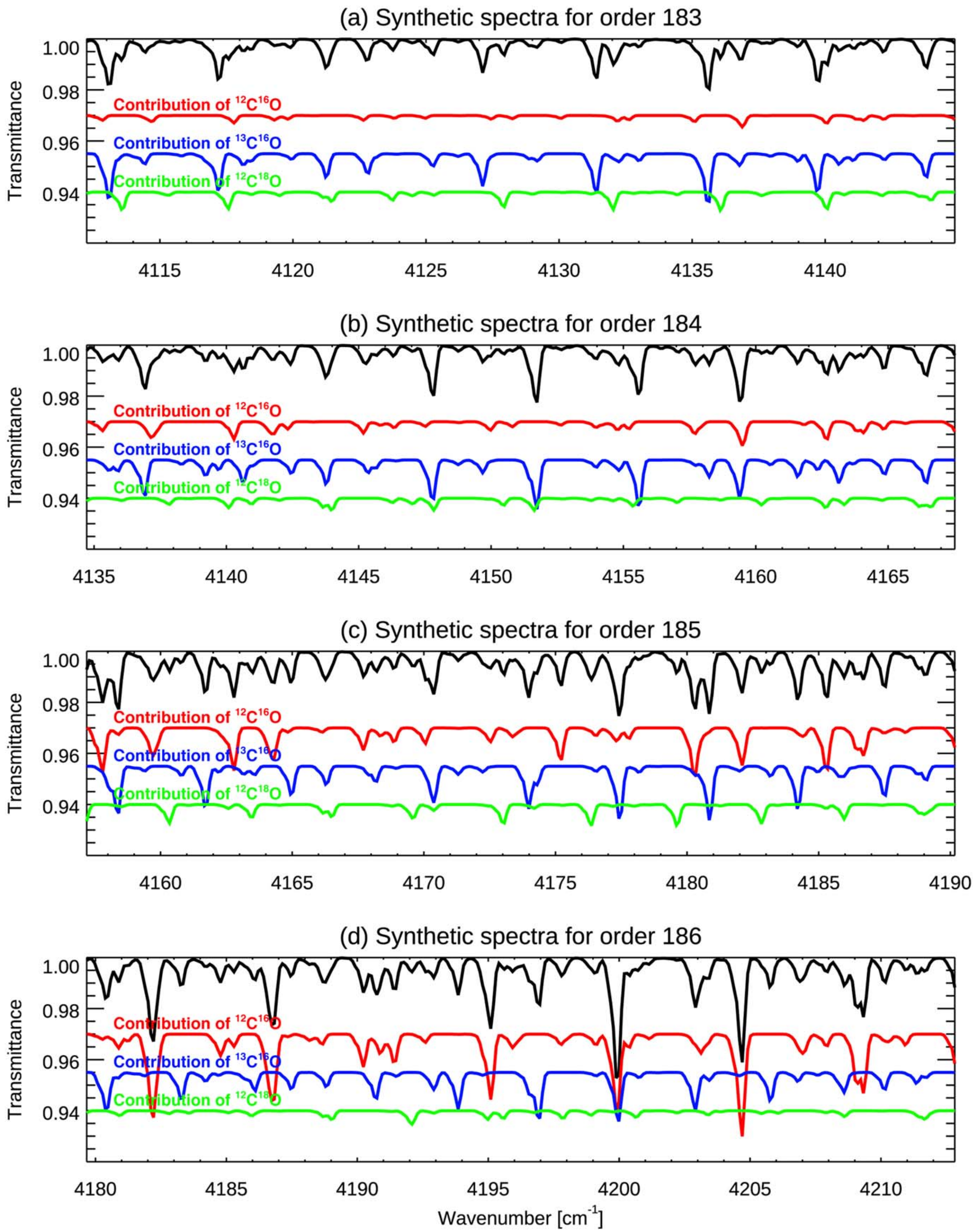

Figure 1. Synthetic spectra of the NOMAD measurements taken with diffraction order 183 (a), order 184 (b), order 185 (c), and order 186 (b) around 30 km tangent height. The assumed vertical profile of total CO volume mixing ratio is 1000 ppm (uniform) and along the line of sight. The isotopic ratios defined in the HITRAN2020 databases are assumed. The red, blue, and green curves illustrate contributions due to $^{12}C^{16}O$, $^{13}C^{16}O$, and $^{12}C^{18}O$ absorption lines. The origin of the *Y*-axis for the red, blue, and green curves have been offset to improve visibility.

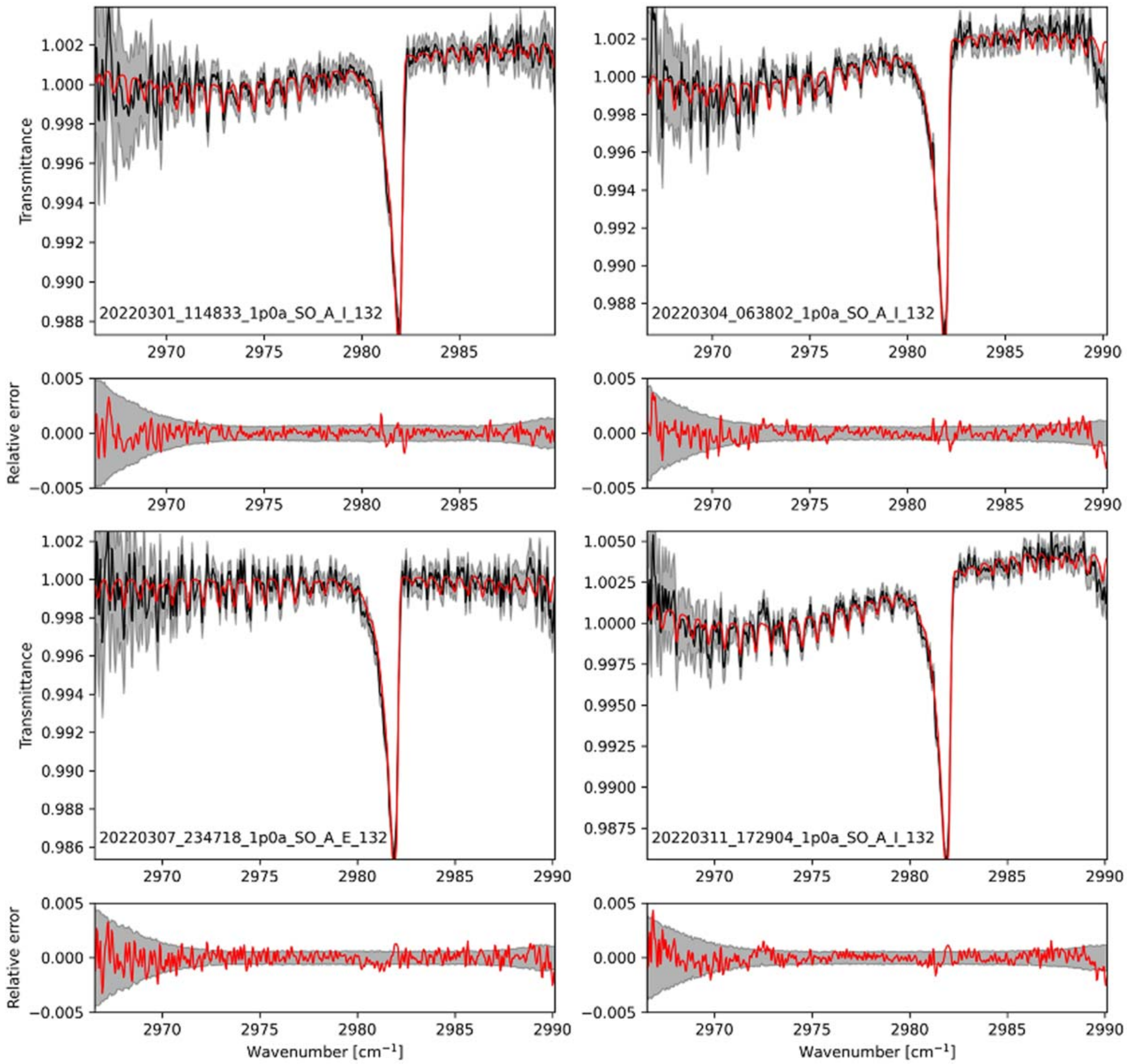

Figure 2. Examples of the NOMAD spectra measured by diffraction order 132 around 30 km tangent height (black) and the best-fit synthetic spectra (red). The bottom small panels show the differences between the observed spectra and the best-fit synthetic spectra in red curves and the instrumental noise level in black.

Table 1
List of the TGO/NOMAD Orbits and Their Geometry Information Analyzed in This Study

Filename	Latitude	Longitude	Local Time	*Ls*
20220301_114833_1p0a_SO_A_I	−79.4	61.2	5.6	182.790
20220304_063802_1p0a_SO_A_I	−84.1	154.1	4.8	184.375
20220307_001142_1p0a_SO_A_E	57.3	−60.2	6.3	185.936
20220307_234718_1p0a_SO_A_E	59.6	−43.8	6.3	186.500
20220311_172904_1p0a_SO_A_I	−83.8	−62.9	20.4	188.654
20220331_214359_1p0a_SO_A_E	80.8	−73.1	11.0	200.493
20220407_050322_1p0a_SO_A_E	79.6	−99.3	12.5	204.266
20220408_175248_1p0a_SO_A_I	1.46	164.3	18.0	205.191

Note. Latitude, longitude, and local time given in this table are those at the tangent point of the line of sight.

retrieval is attempted when the baseline level is lower than 0.5 in transmittance. Therefore, this lower limit varies following seasons and latitudes. Some examples of fit for diffraction order 132 are provided in Figure 2. The vertical resolution on the temperature profiles is on average around 1.6 km and the uncertainty is about 5 K, which is the total error including the regularization error and the retrieval noise error (Trompet et al. 2022a). A comparison between the NOMAD temperature retrievals and those by the Mars Climate Sounder (MCS) on board the Mars Reconnaissance Orbiter shows that the difference is within 5 K (see Figure 2 of Trompet et al. 2022b). Even though the number of the orbits for the comparison is not so large (only 47 profiles), it suggests that if there is a systematic bias in the temperature retrievals, which should be less than 5 K. The upper boundary of the temperature

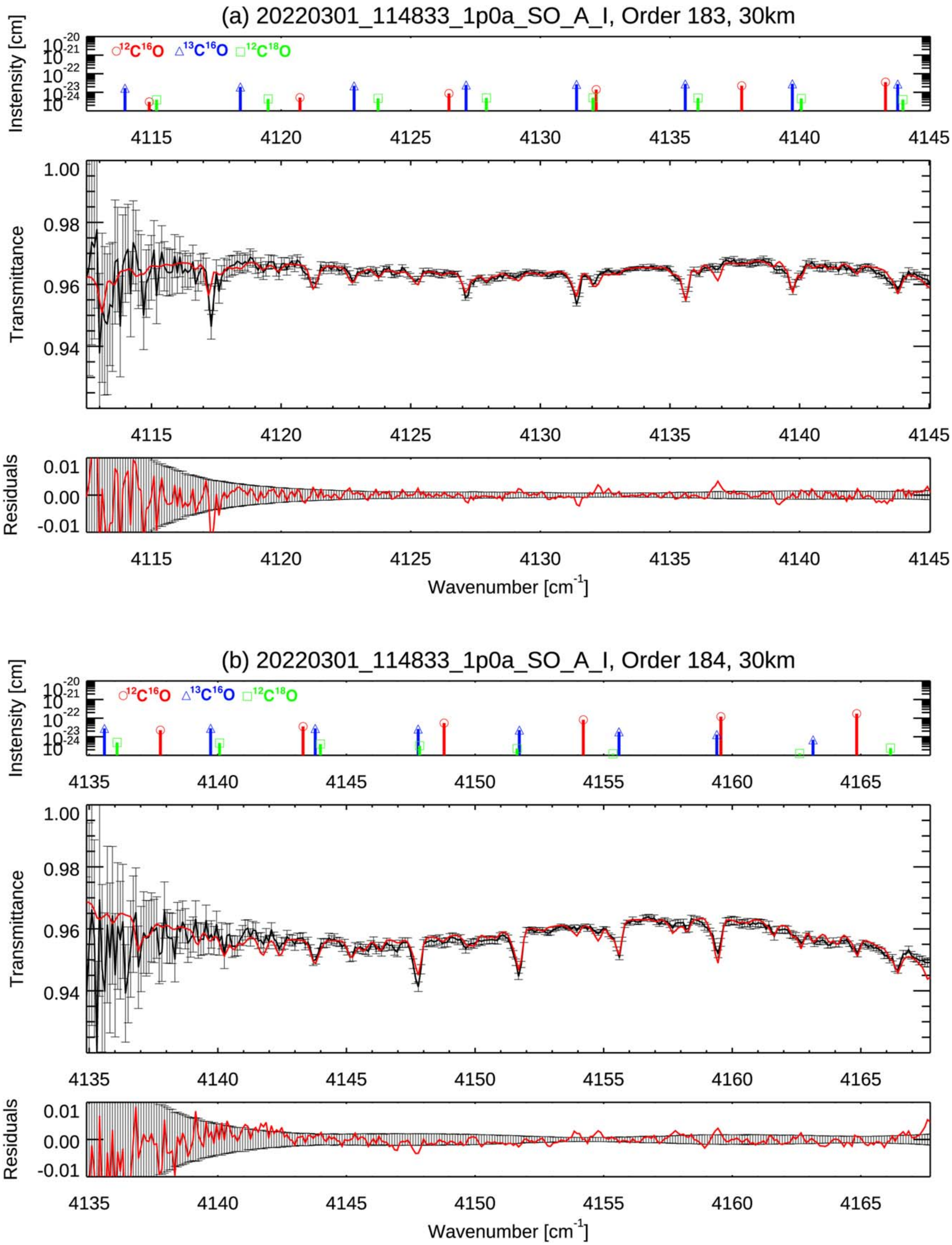

Figure 3. Example of spectra measured by TGO/NOMAD (black curves) in diffraction order 183 (a), order 184 (b), order 185 (c), and order 186 (d). These spectra are measured around 30 km tangential height on 2022 March 1st (the first orbit shown in Table 1). The red curves show the best-fit synthetic spectra. The continuum transmittance is around 0.97, due to the extinction by the aerosols presented along the line of sight. The top small panels show the line intensities of $^{12}C^{16}O$ (red with circular symbols), $^{13}C^{16}O$ (blue with triangle symbols), and $^{12}C^{18}O$ (green with square symbols) in the main diffraction order obtained from HITRAN2020 database. The small bottom panels illustrate the residuals of the top panel in red and the instrumental noise level in black. The residuals are usually within the instrumental noise level, except for some features that come from nearby diffraction orders (these features are present due to the nature of the AOTF transfer function).

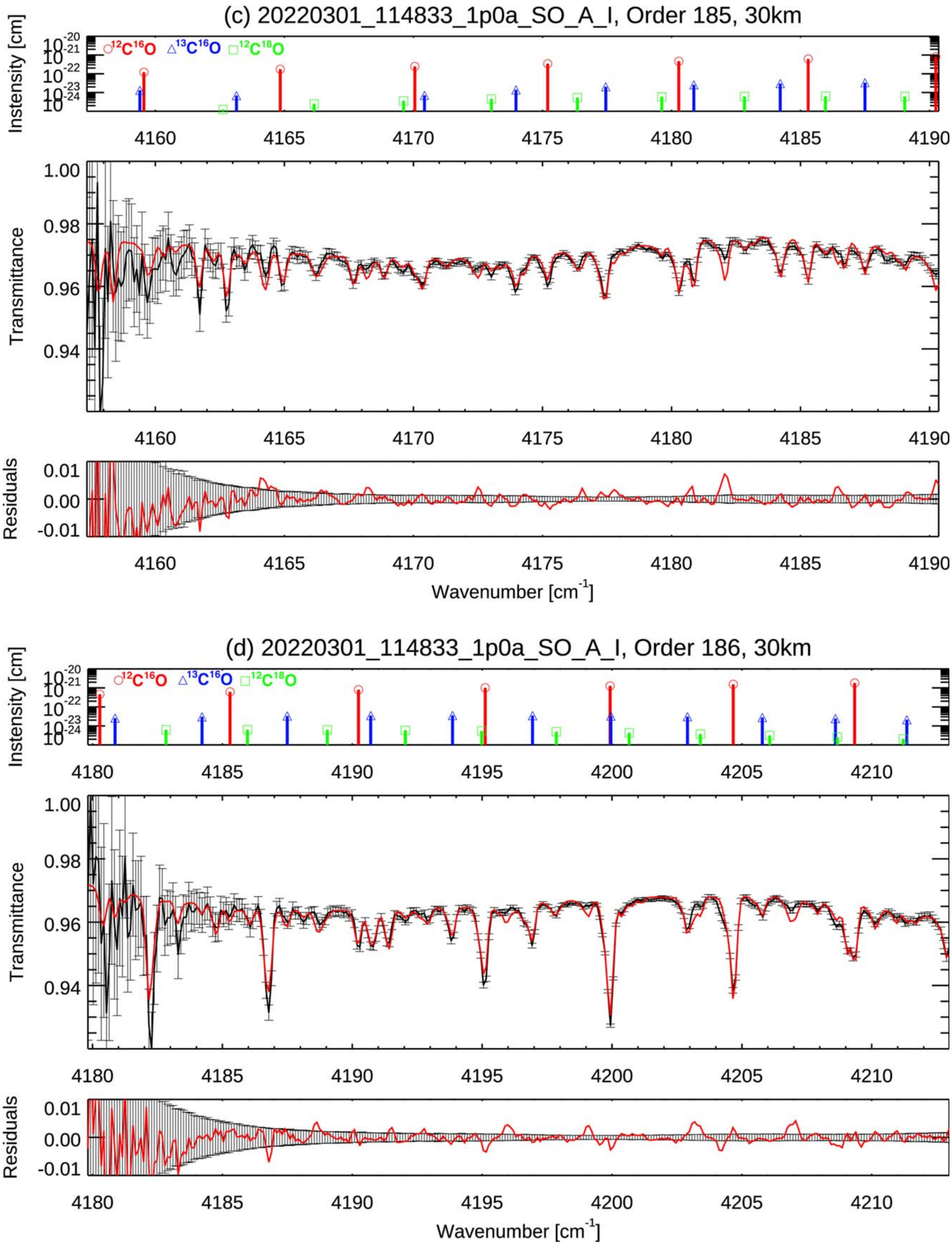

Figure 3. (Continued.)

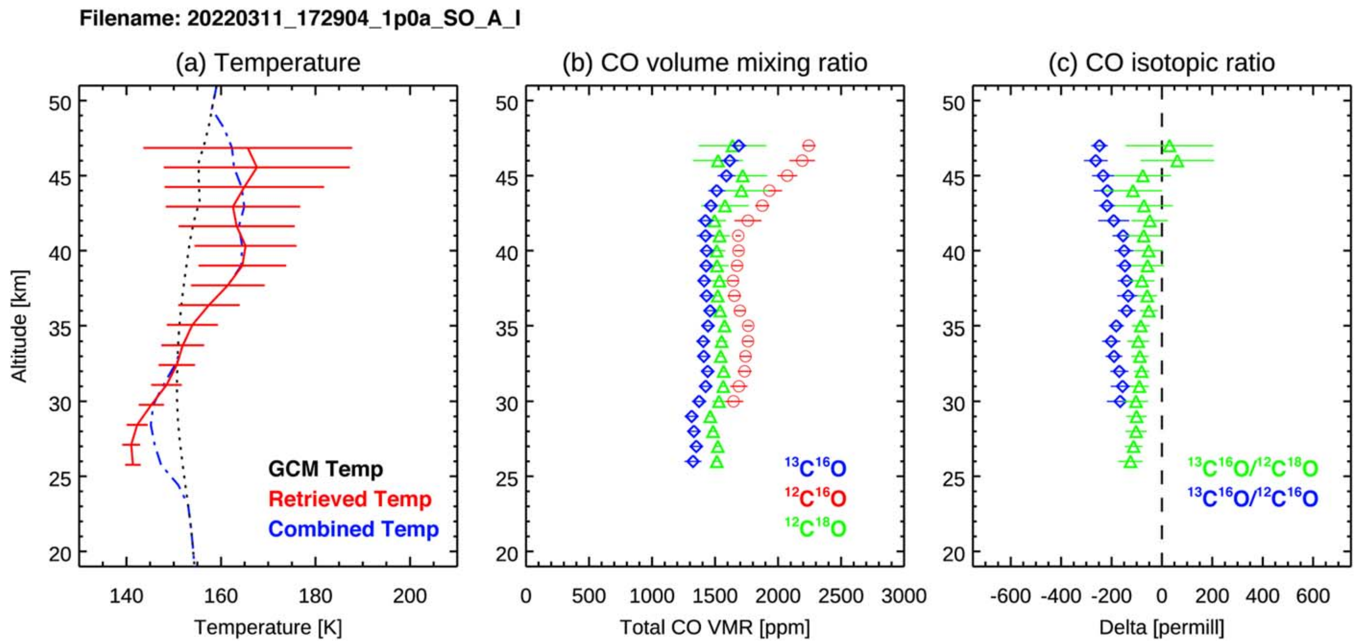

Figure 4. Vertical profile of the temperature profiles (a), volume mixing ratio of $^{12}C^{16}O$ (red with circular symbols), $^{13}C^{16}O$ (blue with square symbols), $^{12}C^{18}O$ (green with triangle symbols) (b), and δ values calculated with $^{13}C^{16}O/^{12}C^{16}O$ ratios (blue with square symbols) and $^{13}C^{16}O/^{12}C^{18}O$ ratios (green with triangle symbols) (c). These profiles are retrieved from the orbit taken on 2022 March 11 (the fifth orbit shown in Table 1). The results from the other orbits are shown in Figure B1. In the panel (a), the red-solid curve, black-dotted curve, and the blue-dashed curves represent temperature profiles retrieved from order 132, predicted by GEM-Mars model, and combined with retrieval and GEM-Mars model, respectively. The x-axis of the panel (b) is the total CO volume mixing ratio retrieved from $^{12}C^{16}O$, $^{13}C^{16}O$, or $^{12}C^{18}O$ lines by assuming the terrestrial isotopic ratio. In other words, the retrieved volume mixing ratios of $^{12}C^{16}O$, $^{13}C^{16}O$, or $^{12}C^{18}O$ are multiplied by the terrestrial isotopic ratios (9.86544×10^{-1}, 1.10836×10^{-2}, and 1.97822×10^{-3}, respectively). The red, blue, and green curves would be overlapped if δ value is 0‰.

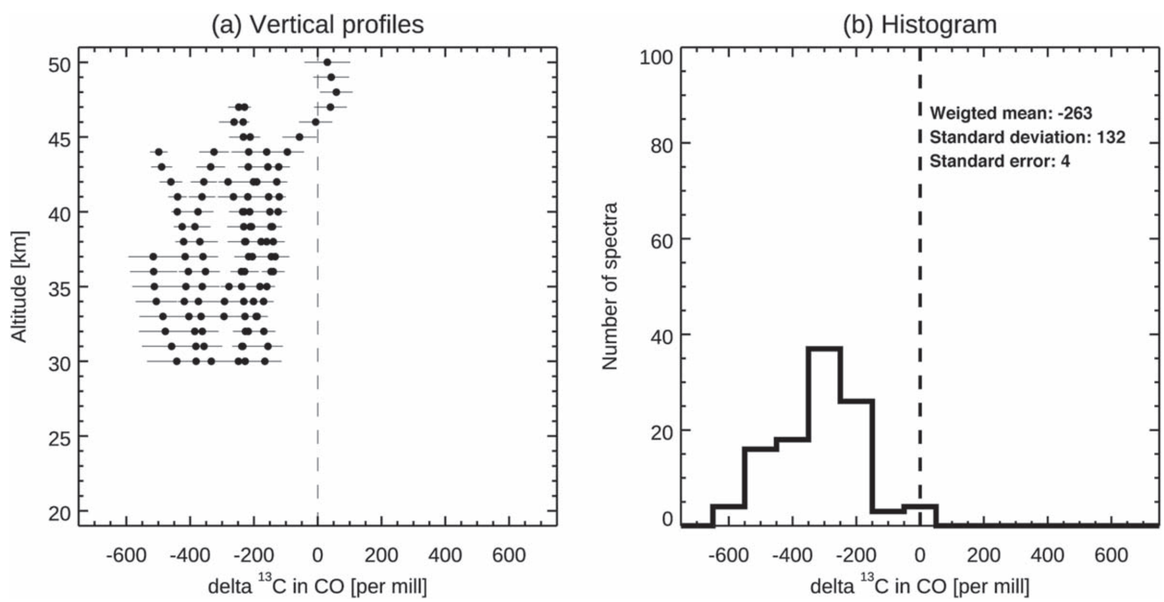

Figure 5. Vertical profiles (a) and histogram (b) of δ ^{13}C values in CO obtained with $^{12}C^{16}O$ and $^{13}C^{16}O$ volume mixing ratio retrieved with original AOTF transfer function and temperature profiles.

profiles (z_{top}) is controlled by the disappearance of the CO_2 lines, while the lower boundary (z_{bot}) is controlled by the reduction of the baseline due to the aerosols or the saturation of the CO_2 lines (see Supp. information of Trompet et al. 2022a). Most of the information in the retrieved CO abundances come from the few km above the tangent altitude (about 70% of the slant number density integrated over the LOS is within 4 km from the tangent height), thus the temperature profiles obtained from order 132 cover the essential altitude range. For the calculation with the radiative transfer model, since it needs a full vertical profile of temperature, we build a full profile $\hat{x}$ from the ground to around 120 km with the retrieved profile x and a GEM-Mars profile x_a simulated for the time and location of the occultation with the formula:

$$\hat{x} = x_a + A(x - x_a)$$

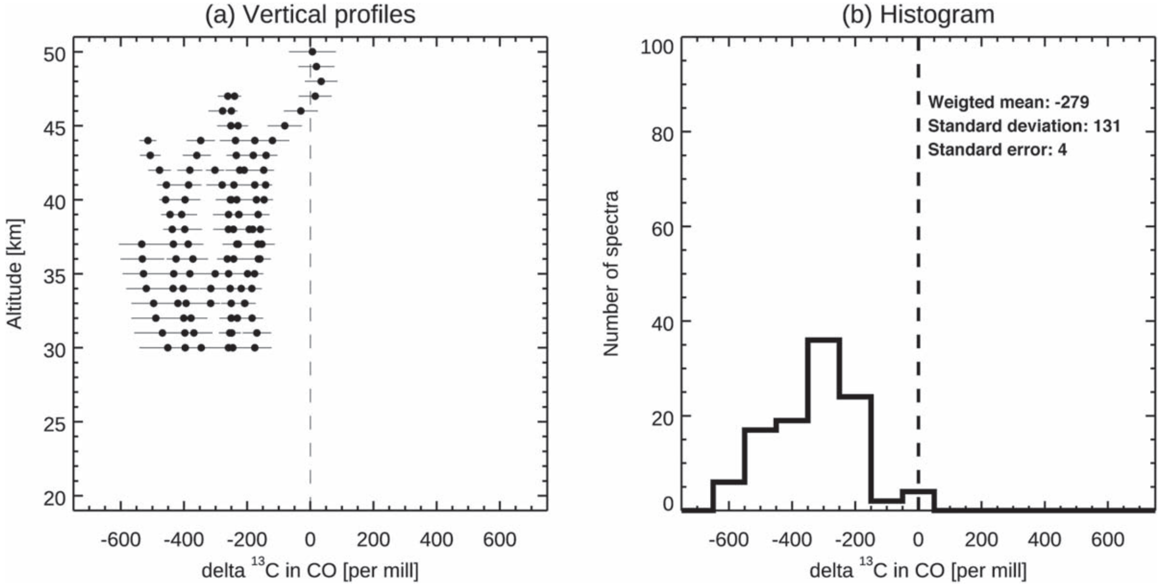

Figure 6. Vertical profiles (a) and histogram (b) of δ ^{13}C values in CO obtained with $^{12}C^{16}O$ and $^{13}C^{16}O$ volume mixing ratio retrieved with original temperature profiles and AOTF transfer function shifted by its uncertainty in the positive direction.

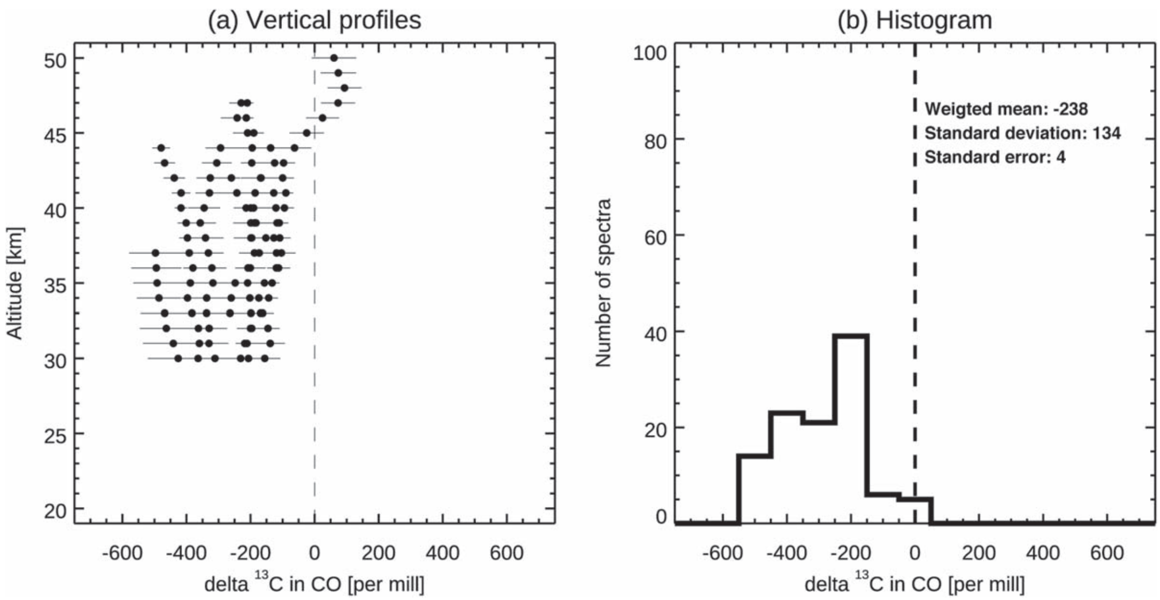

Figure 7. Vertical profiles (a) and histogram (b) of δ ^{13}C values in CO obtained with $^{12}C^{16}O$ and $^{13}C^{16}O$ volume mixing ratio retrieved with original temperature profiles and AOTF transfer function shifted by its uncertainty in the negative direction.

where A is a matrix built as:

$$A_{ij} = \begin{cases} 0_{ij} & \text{if } z_i > z_{\text{top}} \vee z_i < z_{\text{bot}} \\ \delta_{ij} & \text{if } z_{\text{bot}} + 10 < z_i < z_{\text{top}} - 10 \\ \max\left(0, \dfrac{1 - \frac{|z_j - z_i|}{z_i - z_{\text{bot}}}}{z_i - z_{\text{bot}}}\right) & \text{if } z_{\text{bot}} < z_i < z_{\text{bot}} + 10 \\ \max\left(0, \dfrac{1 - \frac{|z_j - z_i|}{z_{\text{top}} - z_i}}{z_{\text{top}} - z_i}\right) & \text{if } z_{\text{top}} - 10 < z_i < z_{\text{top}}. \end{cases}$$

The integral of each row of A is equal to one and the triangular function at the bounds of the retrieved profile serves to smooth the combination of the profiles. Some examples of the combined profiles are provided in Figures 4 and B1.

For the retrievals of CO abundances, the same methodology as the previous water vapor and HCl studies with the NOMAD SO data is applied (Aoki et al. 2019, 2021, 2022). We performed the retrievals for the measurements taken below 50 km because above this altitude the noise exceeds the depth of the absorption features. Only CO and CO_2 molecular absorptions are considered in the radiative transfer calculation. The absorption coefficients are calculated by the line-by-line method with the HITRAN2020 spectroscopic parameters that correct pressure-broadening coefficients for CO_2 atmosphere (Gordon et al. 2022). The vertical profiles of pressure and CO_2 volume mixing ratio in the radiative transfer calculation are obtained from the Global Environmental Multiscale Mars (GEM-Mars) model (Daerden et al. 2019) and those of

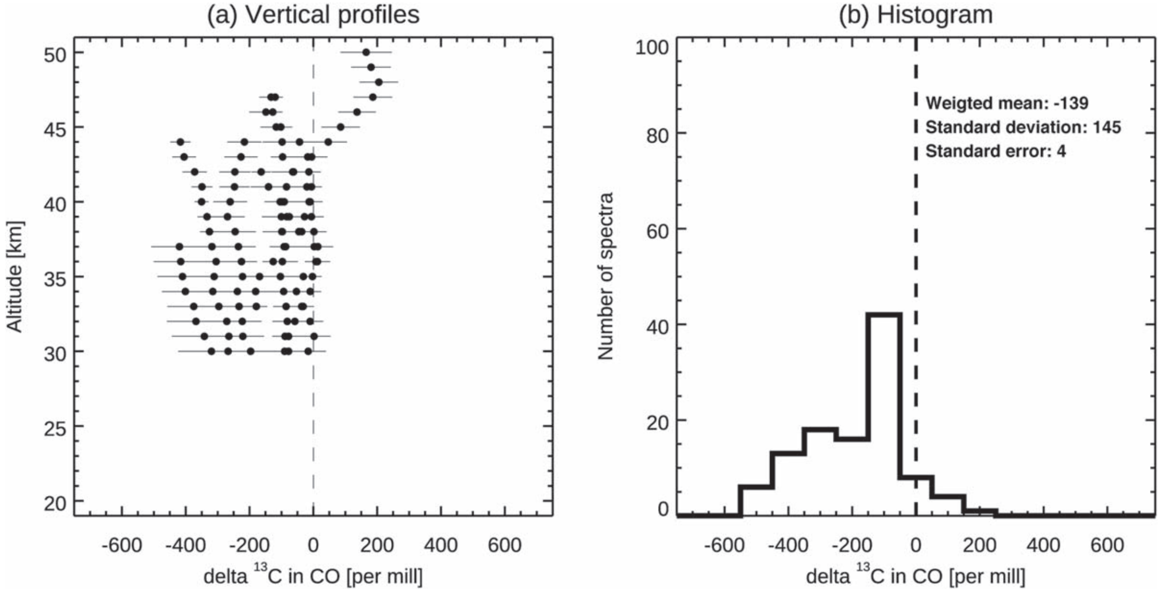

Figure 8. Vertical profiles (a) and histogram (b) of $\delta\,^{13}C$ values in CO obtained with $^{12}C^{16}O$ and $^{13}C^{16}O$ volume mixing ratio retrieved with original AOTF transfer function and temperature profiles shifted by +5 K.

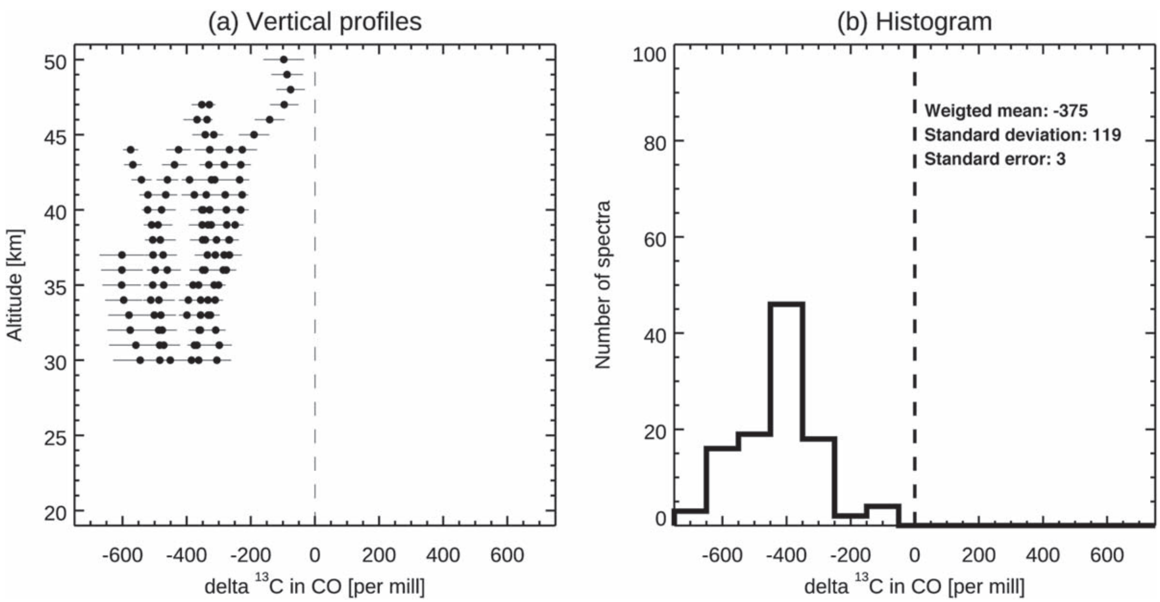

Figure 9. Vertical profiles (a) and histogram (b) of $\delta\,^{13}C$ values in CO obtained with $^{12}C^{16}O$ and $^{13}C^{16}O$ volume mixing ratio retrieved with original AOTF transfer function and temperature profiles shifted by −5 K.

temperature are obtained from the CO_2 retrievals using order 132. The vertical coordinate is defined by height above the Mars geoid (Lemoine et al. 2001). The field of view measured by the NOMAD SO channel is recorded on 16 detector rows, which are split into four discrete "bins" of four rows each. Therefore, four spectra are acquired simultaneously and returned individually. The retrievals are processed for each bin and every single spectrum taken at a tangential altitude by assuming a constant volume mixing ratio along the line of sight (in other words, the $^{12}C^{16}O$, $^{13}C^{16}O$, and $^{12}C^{18}O$ column densities along the line of sight are retrieved). The retrieved CO abundances are finally averaged on a common vertical grid with an interval of 1 km to reduce the uncertainties from random variations. The standard deviation of the retrieved CO abundances within 1 km altitudes provides a realistic relative uncertainty of the obtained CO abundances due to the instrumental random photon noise.

To reduce the uncertainty in the obtained isotopic ratio, we perform the retrievals simultaneously with the spectra recorded in the four different diffraction orders: order 186 (4180–4213 cm^{-1}), order 185 (4157–4190 cm^{-1}), order 184 (4134–4167 cm^{-1}), and order 183 (4112–4145 cm^{-1}). Figure 3 shows examples of the data analysis for these four spectral ranges. The agreements between the best-fit synthetic spectra and the measured spectra are generally good and within the instrumental random photon noise, except for a few features that are attributed to contamination from adjacent orders.

The major sources of errors in the retrieved isotopic ratio are (1) the instrumental random photon noise, (2) uncertainty in the temperature profile assumed in the radiative transfer

Table 2
List of the CO Isotopic Ratios Obtained by the Analysis of the TGO/NOMAD Presented in This Paper and Calculated by the One-dimensional Photochemical Model Reported in Yoshida et al. (2023)

Type of the NOMAD Retrievals	Mean δ Values	Standard Deviation of the Mean	Standard Error of the Mean	Photochemical Model (Yoshida et al. 2023)
$^{13}C^{16}O/^{12}C^{16}O$ ratios with original AOTF and temperature	−263‰	132‰	4‰	From −165 to −117‰ (with vertical transport) and from −225 to −178‰ (without vertical transport)
$^{13}C^{16}O/^{12}C^{16}O$ ratios with AOTF function shifted positive Direction	−279‰	131‰	4‰	
$^{13}C^{16}O/^{12}C^{16}O$ ratios with AOTF function shifted negative direction	−238‰	134‰	3‰	
$^{13}C^{16}O/^{12}C^{16}O$ ratios with temperature shifted by +5 K	−139‰	145‰	4‰	
$^{13}C^{16}O/^{12}C^{16}O$ ratios with temperature shifted by −5 K	−375‰	119‰	3‰	
$^{13}C^{16}O/^{12}C^{18}O$ ratios with AOTF and temperature	−82‰	60‰	5‰	…
$^{13}C^{16}O/^{12}C^{18}O$ ratios with AOTF function shifted positive direction	−69‰	70‰	5‰	
$^{13}C^{16}O/^{12}C^{18}O$ ratios with AOTF function shifted negative direction	−98‰	55‰	4‰	
$^{13}C^{16}O/^{12}C^{18}O$ ratios with temperature shifted by +5 K	−88‰	58‰	4‰	
$^{13}C^{16}O/^{12}C^{18}O$ ratios with temperature shifted by −5 K	−77‰	64‰	5‰	

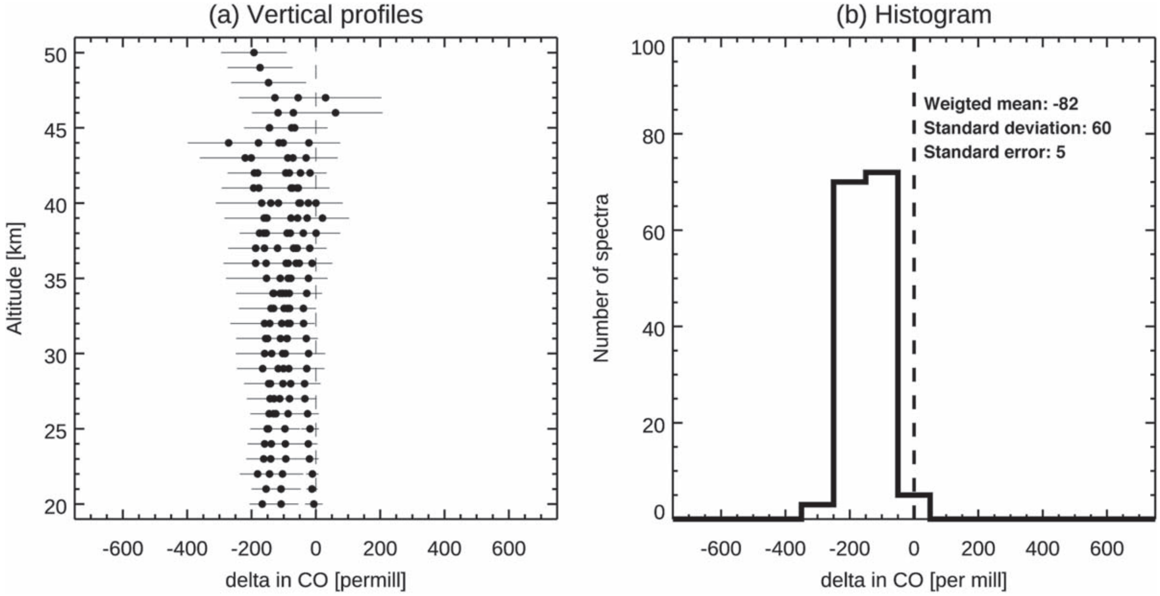

Figure 10. Vertical profiles (a) and histogram (b) of δ values in CO obtained with $^{12}C^{18}O$ and $^{13}C^{16}O$ volume mixing ratio retrieved with original AOTF transfer function and temperature profiles.

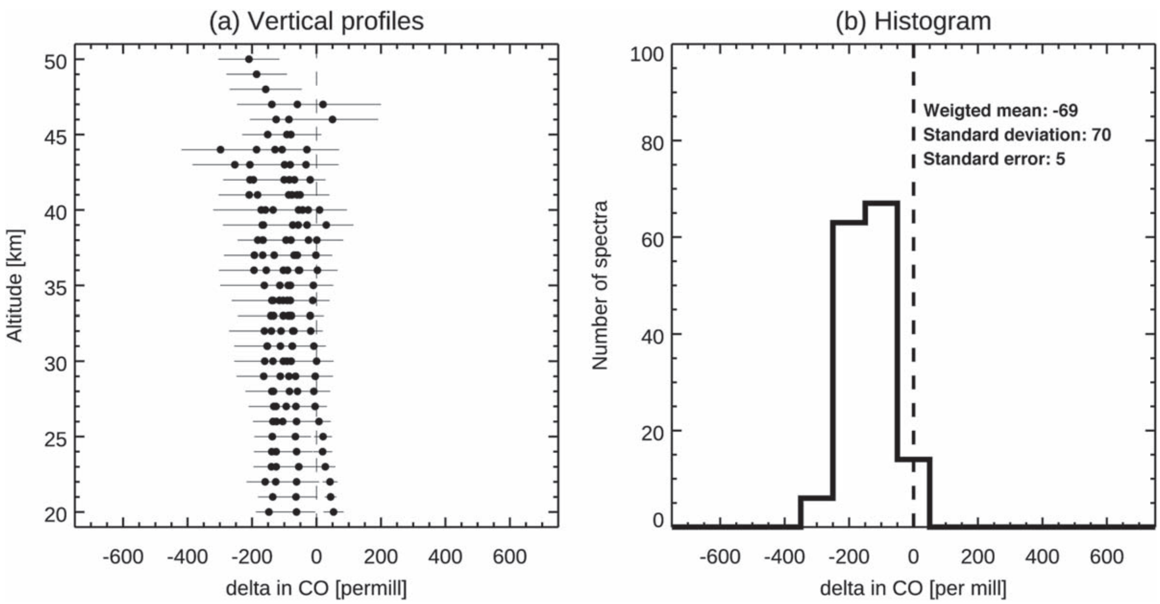

Figure 11. Vertical profiles (a) and histogram (b) of δ value in CO obtained with $^{18}C^{16}O$ and $^{13}C^{16}O$ volume mixing ratio retrieved with original temperature profiles and AOTF transfer function shifted by its uncertainty in the positive direction.

calculations, and (3) uncertainty in the AOTF transfer function. The error in the retrieved CO abundances due to instrumental photon noise can be evaluated from the standard deviation when the retrieved CO abundances from each spectrum are averaged within 1 km (there are 3–12 spectra for each 1 km interval). Based on the retrievals, the CO isotopic ratios ($^{12}C^{16}O/^{13}C^{16}O$, $^{12}C^{18}O/^{13}C^{16}O$) are calculated for every 1 km for each orbit. The final results are provided by their weighted mean. The random error in the final isotopic ratios due to the instrumental random photon noise and temperature uncertainty can be obtained by the standard deviation and standard error of the mean. Meanwhile, the systematic error in the final isotopic ratios of CO is difficult to estimate. Uncertainty in the AOTF transfer function and a possible systematic error in the temperature retrievals are candidates for the sources of the systematic error in the isotopic ratios in CO. To estimate the magnitude of these systematic errors, we perform the retrievals with temperature profiles and the AOTF transfer functions shifted by their uncertainty. Possible systematic error in the temperature retrievals is within 5 K, as described above, and thus we perform the retrievals with temperature profiles shifted by $\pm$5 K. The uncertainty of the AOTF transfer function can be estimated from the standard deviation when four parameters to characterize the AOTF transfer function are determined by fitting with second orders of polynomial function (Figure FA1 in Villanueva et al. 2022, see also the the AOTF transfer function for order 185 of the NOMAD SO channel shown in Figure A3 in Appendix A).

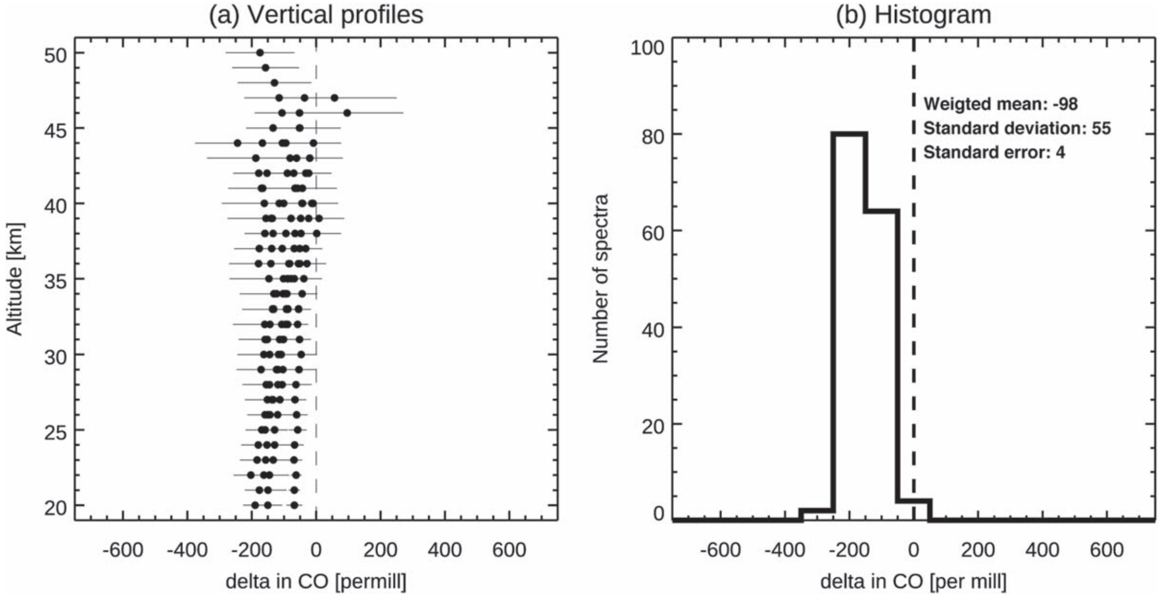

Figure 12. Vertical profiles (a) and histogram (b) of δ value in CO obtained with $^{18}C^{16}O$ and $^{13}C^{16}O$ volume mixing ratio retrieved with original temperature profiles and AOTF transfer function shifted by its uncertainty in the negative direction.

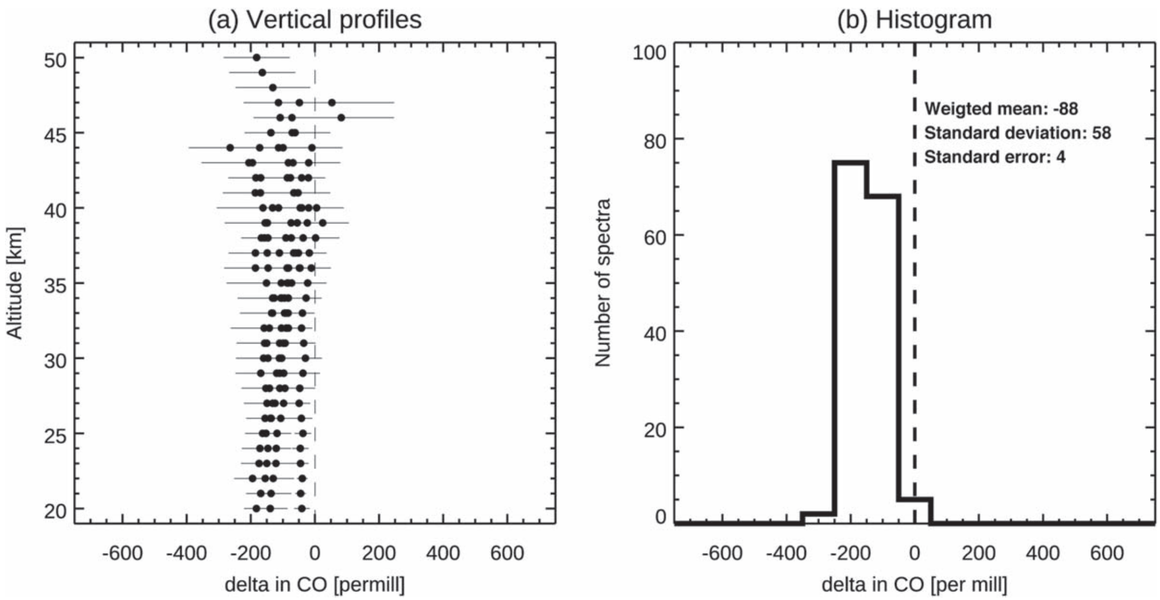

Figure 13. Vertical profiles (a) and histogram (b) of δ values in CO obtained with $^{12}C^{18}O$ and $^{13}C^{16}O$ volume mixing ratio retrieved with original AOTF transfer function and temperature profiles shifted by +5 K.

3. Results and Discussion

Figure 4 shows an example of the retrieved vertical profiles of temperature, $^{12}C^{16}O$, $^{13}C^{16}O$, and $^{12}C^{18}O$ volume mixing ratio, and the isotopic ratios. CO retrievals are only performed for those altitudes where temperature retrievals from order 132 are available. The lower limits of the vertical profiles of $^{12}C^{16}O$ and $^{13}C^{16}O$ are defined as 30 km and 20 km, respectively, unless the lower limit of the temperature retrievals is above these altitudes, because the optical depth along the line of sight for the lines reaches very high values below these altitudes. Figure 5 shows the calculated $\delta\ ^{13}C$ values based on the retrieved $^{12}C^{16}O$ and $^{13}C^{16}O$ volume mixing ratio at each altitude. Figure 5(a) presents the vertical profiles of the obtained $\delta\ ^{13}C$ values and Figure 5(b) shows their histogram. The weighted mean value of the $\delta\ ^{13}C$ values is −263‰. Standard deviation and standard error of the mean are 132‰ and 4‰, respectively, which represent the uncertainty in the obtained $\delta\ ^{13}C$ value due to instrumental photon noise and random error in the retrieved temperature (note that the standard error of the mean, which is derived by the division between standard deviation and the square root of the number of samples, reflects the uncertainty in the mean value). Apart from these random error sources, the uncertainty in the AOTF transfer function and possible systematic error in the retrieved temperature profiles are candidates of the systematic errors in the retrieved $\delta\ ^{13}C$ value. To estimate the magnitude of these systematic errors, the same retrievals are performed with either the temperature profiles shifted by ±5 K or the AOTF transfer functions shifted by their uncertainties. Figures 6 and 7 show the vertical profiles and histograms of the $\delta\ ^{13}C$ values retrieved

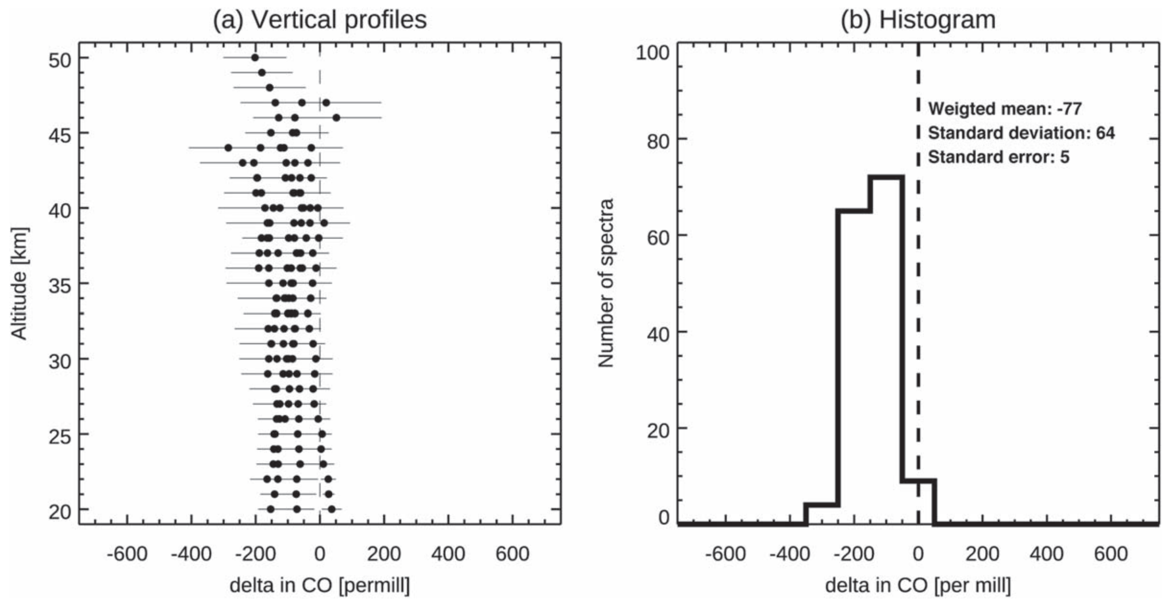

Figure 14. Vertical profiles (a) and histogram (b) of δ values in CO obtained with $^{12}C^{18}O$ and $^{13}C^{16}O$ volume mixing ratio retrieved with original AOTF transfer function and temperature profiles shifted by −5 K.

with the AOTF transfer function shifted by their uncertainty, and Figures 8 and 9 present those retrieved with the temperature profiles shifted by ±5 K. Table 2 summarizes these obtained $\delta\ ^{13}C$ values with original and shifted temperature profiles and AOTF transfer functions. The weighted mean values of the $\delta\ ^{13}C$ values can be changed by ∼20‰ due to systematic uncertainty in the AOTF transfer function, and by ∼120‰ due to a possible systematic error in the retrieval temperature profiles. Despite the relatively large uncertainties due to temperature, the result suggests a depletion of ^{13}C in CO.

The temperature assumed in the radiative transfer calculation has a large impact on the obtained $\delta\ ^{13}C$. This is primary due to the fact that the $^{12}C^{16}O$ lines are quite sensitive to temperature. We also examine the $^{13}C^{16}O/^{12}C^{18}O$ ratio to obtain further information because these lines are less sensitive to temperature. Figure 10 shows the vertical profiles and histogram of δ values in CO between 20 and 50 km based on the retrieved volume mixing ratio of $^{13}C^{16}O$ and $^{12}C^{18}O$. The δ values that are shown here calculated by the same equation for $\delta\ ^{13}C$ except that $^{12}C^{18}O$ is used instead of $^{12}C^{16}O$:

$$\delta = \left[\frac{(^{13}C^{16}O/^{12}C^{18}O)_{Mars}}{(^{13}C^{16}O/^{12}C^{18}O)_{Earth}} - 1\right] \times 1000‰$$
$$= \left(\frac{\delta^{13}C \times 10^{-3} + 1}{\delta^{18}O \times 10^{-3} + 1} - 1\right) \times 1000‰, \qquad (1)$$

where $(^{13}C^{16}O/^{12}C^{18}O)_{Mars}$ is the retrieved isotopic ratio, and $(^{13}C^{16}O/^{12}C^{18}O)_{Earth}$ is the ratio between isotopic ratios of the terrestrial atmosphere defined in HITRAN2020 database ($(^{13}C^{16}O/^{12}C^{18}O)_{Earth} = 5.5899$ (Gordon et al. 2022). Note that HITRAN2020 uses V-PDB for carbon and Vienna Standard Mean Ocean Water (V-SMOW) for oxygen as the references). The weighted mean of the obtained δ values is −82‰, and the standard deviation and standard error of the mean are 60‰ and 5‰, respectively. Figures 11–14 show the vertical profiles and histogram of the δ values retrieved with the AOTF transfer function shifted by their uncertainty (Figures 11 and 12) and the temperature profile shifted by ±5 K (Figures 13 and 14). Table 2 also summarizes the obtained δ values with the original and shifted temperature profiles or AOTF transfer functions. The weighted mean of the obtained δ values can be changed by ∼15‰ due to systematic uncertainty in the AOTF transfer function and by ∼5‰ due to a possible systematic error in the retrieval temperature profiles. This shows that the δ values obtained with $^{13}C^{16}O/^{12}C^{18}O$ are much less sensitive to temperature when compared to the $\delta\ C^{13}$ values obtained with $^{13}C^{16}O/^{12}C^{16}O$. However, by definition, the δ values that obtained here are affected by both carbon and oxygen fractionation, and the oxygen isotopic composition of CO in the Martian atmosphere is uncertain. Schmidt et al. (2013) suggested that the photolysis of CO_2 may theoretically induce the depletion of oxygen in CO compared to CO_2, up to about −150‰. Meanwhile, oxides such as O_3 and CO_2 in the Earth's atmosphere are known to be mass independently enriched in ^{17}O and ^{18}O by ∼10‰ through several fractionation processes, such as formation reactions of ozone (e.g., Thiemens 1999). Among the fractionation processes, the photolysis of CO_2 is expected to affect the oxygen isotopic composition of CO dominantly because it is the major source of CO in the Martian atmosphere. Here, assuming that the oxygen isotopic composition of CO is mainly determined through the photolysis of CO_2, both $\delta\ ^{18}O$ and $\delta\ ^{13}C$–$\delta\ ^{18}O$ in CO are negative, as shown by Schmidt et al. (2013), leading to the negative value of δ about −100‰. This is consistent with the measured negative δ value by NOMAD, indicating the depletion of not only ^{18}O but also ^{13}C in CO, as found from the analysis of $^{13}C^{16}O/^{12}C^{16}O$.

The calculation by one-dimensional photochemical model by Yoshida et al. (2023) predicted that the $\delta\ ^{13}C$ can be between −165‰ and −117‰ with vertical transport and between −225‰ and −178‰ without vertical transport at 30–50 km due to the fractionation induced by the photolysis of CO_2.

Despite its relatively large uncertainty, our analysis with the TGO/NOMAD measurements suggests that such a depletion of ^{13}C in CO may actually be present. As shown in Table 2, the measurements and models agree within the error values and observed depletion of ^{13}C in CO is consistent with the CO_2 photolysis-induced fractionation.

CO_2 in the current Mars atmosphere is slightly enriched in ^{13}C as measured by the Curiosity rover ($\delta^{13}C = 46 \pm 4$; Webster et al. 2013). Analysis of the carbonates in the Allan Hills (ALH) 84001 Martian meteorite, which formed ∼4 Ga before present, suggests that the δ ^{13}C value ∼4 Ga before present was already slightly enriched in ^{13}C, estimated to be $+30 \pm 10$‰ (e.g., Niles et al. 2005; Halevy et al. 2011; Shaheen et al. 2015). Compared to these values, the recent discovery of ^{13}C depletion in sedimentary organic carbon at Gale crater (up to about −137‰; House et al. 2022) is quite significant. The results of the analysis with TGO/NOMAD data presented in this study suggest that such a ^{13}C depletion in CO may be induced by photolysis of CO_2. This is consistent with the hypothesis that strong ^{13}C depletion in sedimentary organic carbon, which is difficult to explain only by currently known biological fractionation processes such as methanotrophy (House et al. 2022), is originated by the depletion of ^{13}C in CO. This implies that CO might be more abundant in the early Mars atmosphere and organics might be originated from CO via formaldehyde by photochemical reaction (Lammer et al. 2020).

4. Conclusion

We have analyzed eight orbits of the solar occultation measurements taken by ExoMars-TGO/NOMAD to investigate $^{13}C/^{12}C$ in CO in the atmosphere of Mars. The analysis is performed with the spectra taken with four diffraction orders. The mean δ ^{13}C value obtained from the retrieved $^{13}C^{16}O$ and $^{12}C^{16}O$ volume mixing ratios is −263‰, and the standard deviation and standard error of the mean are 132‰ and 4‰, respectively. This value can be changed by ∼20‰ due to uncertainty in the AOTF transfer function and by ∼120‰ due to possible systematic error in the retrieved temperature profiles. This large uncertainty in the obtained $^{13}C^{16}O/^{12}C^{16}O$ ratio is mainly due to the strong temperature dependence in the $^{12}C^{16}O$ lines. Less temperature-dependent lines of $^{12}C^{18}O$ are used instead of $^{12}C^{16}O$. The mean δ value obtained with the retrieved $^{13}C^{16}O$ and $^{12}C^{18}O$ volume mixing ratios is −82‰, and the standard deviation and standard error of the mean are 59‰ and 4‰, respectively. This value can be changed by ∼15‰ due to uncertainty in the AOTF transfer function and by ∼5‰ due to possible systematic error in the retrieved temperature profiles. With the assumption that ^{18}O in CO is depleted by about −150‰, the δ ^{13}C value obtained by $^{13}C^{16}O/^{12}C^{16}O$ is consistent with the δ value obtained by $^{3}C^{16}O/^{12}C^{18}O$.

Despite the fact that the uncertainties are relatively large, our results suggest a depletion of ^{13}C in CO. This is consistent with the results predicted by a one-dimensional photochemical model (Yoshida et al. 2023), which shows that a fractionation in $^{13}C/^{12}C$ occurs in the photolysis of CO_2. This result might support the hypothesis that the atmosphere of early Mars was CO-rich and the recently discovered depleted ^{13}C in the organic carbon at Gale crater (House et al. 2022) is due to fractionation during the photolysis of CO_2 (Lammer et al. 2020).

This work is supported by JSPS KAKENHI grant Nos. 22H05151, 22K03709, 22H00164, 19H00707. The NOMAD experiment is led by the Royal Belgian Institute for Space Aeronomy (IASB-BIRA), assisted by Co-PI teams from Spain (IAA-CSIC), Italy (INAF-IAPS), and the United Kingdom (Open University). This project acknowledges funding by the Belgian Science Policy Office (BELSPO), with the financial and contractual coordination by the ESA Prodex Office (PEA 4000103401, 4000121493), by Spanish Ministry of Science and Innovation (MCIU) and by European funds under grants PGC2018-101836-B-I00 and ESP2017-87143-R (MINECO/FEDER), as well as by UK Space Agency through grants ST/V005332/1, ST/V002295/1, ST/W00268X/1, and ST/R001405/1 and Italian Space Agency through grant 2018-2-HH.0. This work is supported by the Belgian Fonds de la Recherche Scientifique—FNRS under grant No. 30442502 (ET_HOME) and has received funing from the European Union's Horizon 2020 research and innovation program (grant agreement No. 101004052, RoadMap project). The IAA/CSIC team acknowledges financial support from the State Agency for Research of the Spanish MCIU through the 'Center of Excellence Severo Ochoa' award for the Instituto de Astrofísica de Andalucía (SEV-2017-0709). US investigators were supported by the National Aeronautics and Space Administration. Canadian investigators were supported by the Canadian Space Agency. S.R. thanks BELSPO for the FED-tWIN funding (Prf-2019-077 - RT MOLEXO).

Appendix A
Challenges for the Analysis of the NOMAD Spectra Taken in Orders 183–186

As described in the main body of the text, there are some challenges to work on the NOMAD spectra taken in diffraction orders 183–186. The first challenge is the contamination of the features from adjacent diffraction orders due to the nature of the AOTF transfer function. Figure A1 separately visualizes the contributions from the adjacent orders. As shown in these figures, many features from adjacent orders appear in measured orders 183–186 spectra. The second challenge is the strong temperature dependence of the $^{12}C^{16}O$ lines in the spectral ranges of orders 183–186. Figure A2 shows the E'' parameters of $^{12}C^{16}O$, $^{13}C^{16}O$, and $^{12}C^{18}O$ lines at diffraction orders 183–186 obtained from HITRAN2020 database. As shown in these figures, the values for $^{12}C^{16}O$ lines are particularly high in order 183–185. To estimate the errors in the retrieved CO isotopic ratio due to these uncertainties, the retrievals with temperature profiles or the AOTF transfer function shifted by these uncertainties are performed. The black curve in Figure A3 shows the AOTF transfer function for order 185 calculated by the parameters presented in Villanueva et al. (2022). The AOTF transfer function of the NOMAD SO channel is modeled by the combination of a sinc squared function and a Gaussian function. There are four parameters to characterize these functions (i.e., width of the sinc function, side-lobe factor for the sinc function, asymmetry factor for the sinc function, and the intensity of the Gaussian function, see Villanueva et al. 2022 for details). The most sensitive parameter to the retrieved abundances of trace gases is the last parameter, i.e., the intensity of the Gaussian function, because it changes proportionally to the depth of the absorption features. Thus, we evaluate the uncertainty of this parameter and create the AOTF transfer function shifted by the uncertainty to perform

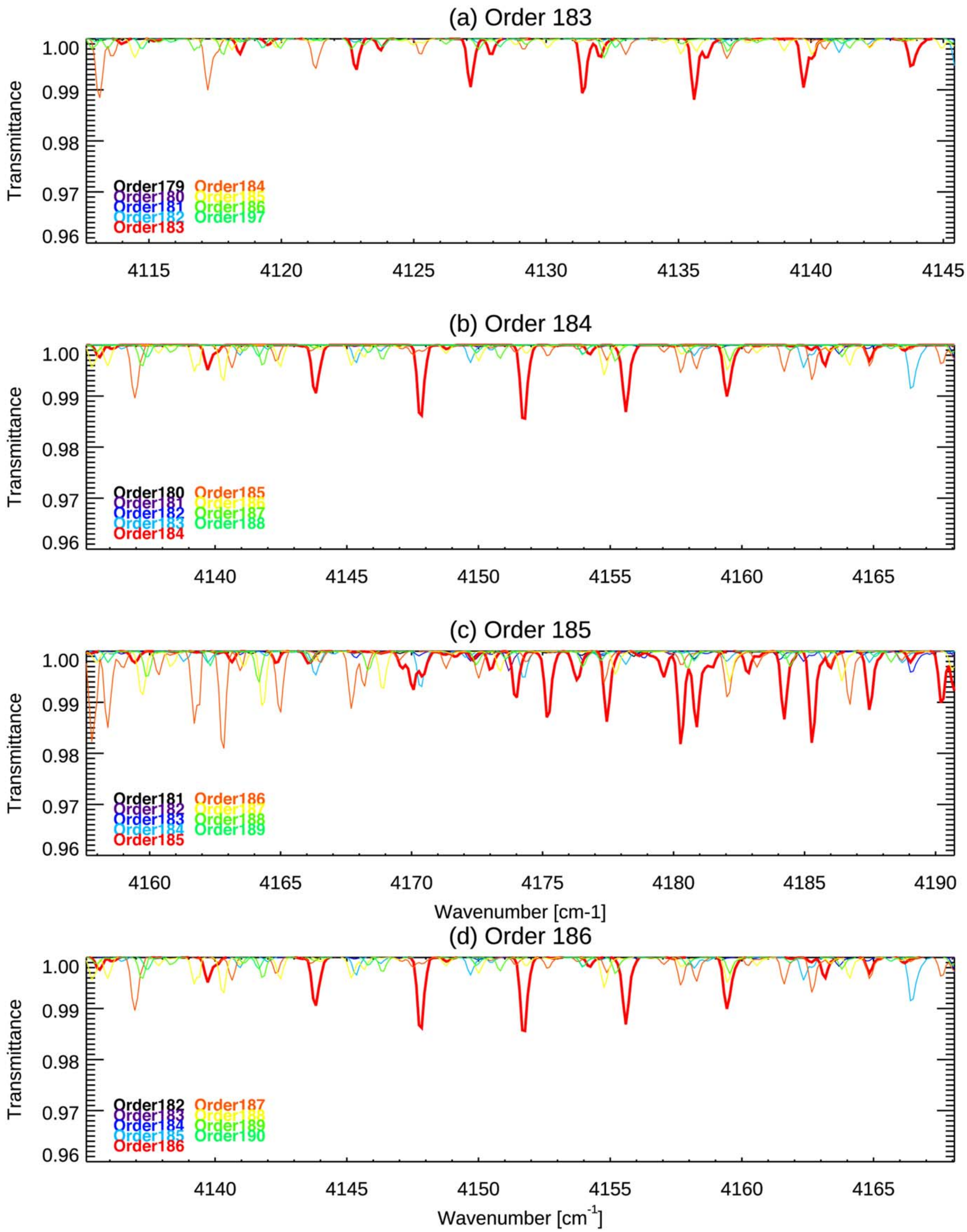

Figure A1. The contribution of the main and adjacent orders appeared in the NOMAD spectra for order 183 (a), order 184 (b), order 185 (c), and order 186 (d). The synthetic spectra are calculated for the measurements around 30 km tangent height. The differences in color and line type represent the contribution of the different diffraction order (the main order contribution is shown as the bold lines in red, and the adjacent orders are shown in the other colors).

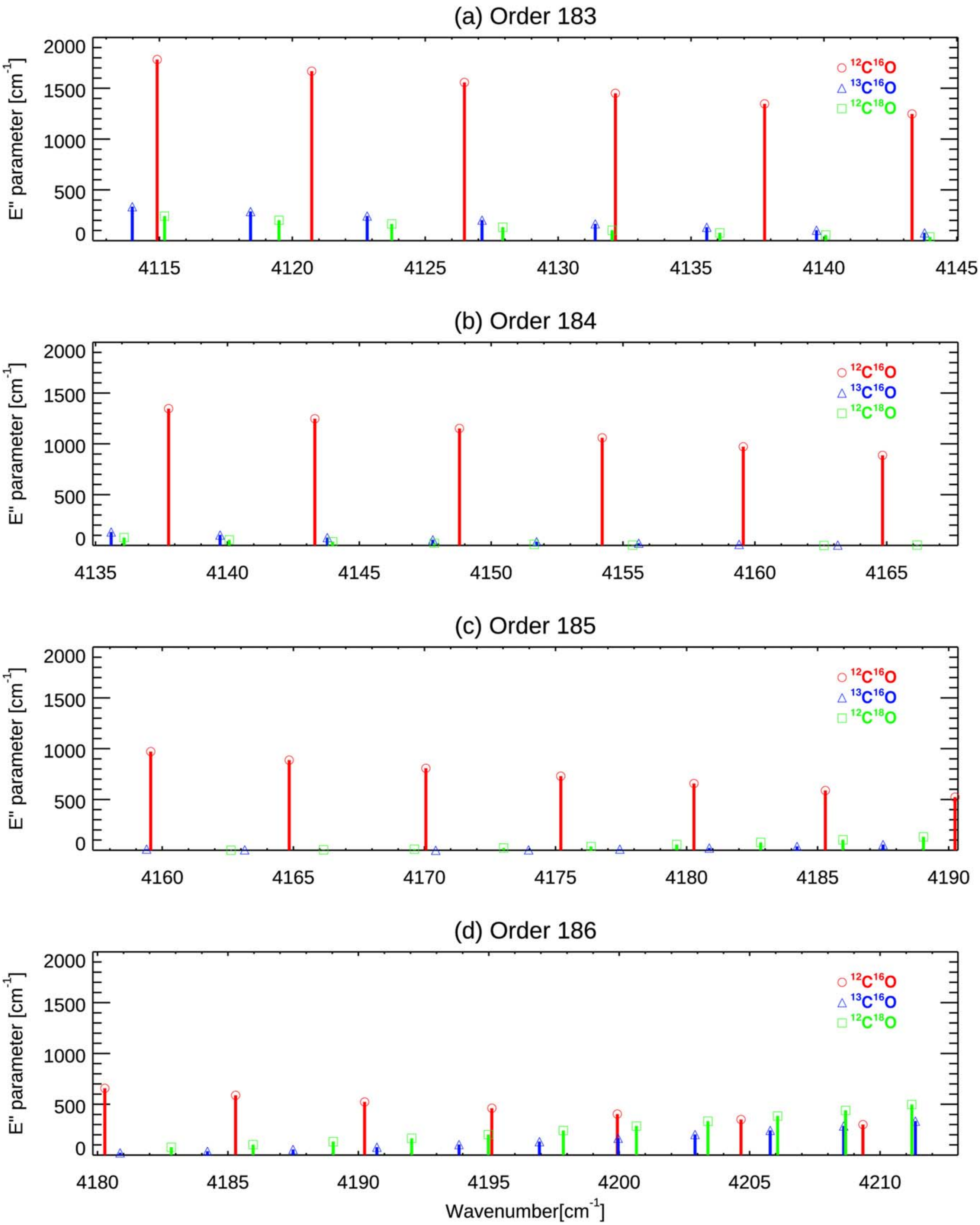

Figure A2. Lower-state energy of the transition (the E'' parameters) of $^{12}C^{16}O$ (red with circular symbols), $^{13}C^{16}O$ (blue with triangle symbols), and $^{12}C^{18}O$ (green with square symbols) lines in diffraction order 183 (a), order 184 (b), order 185 (c), and 186 (d) obtained from HITRAN2020 database.

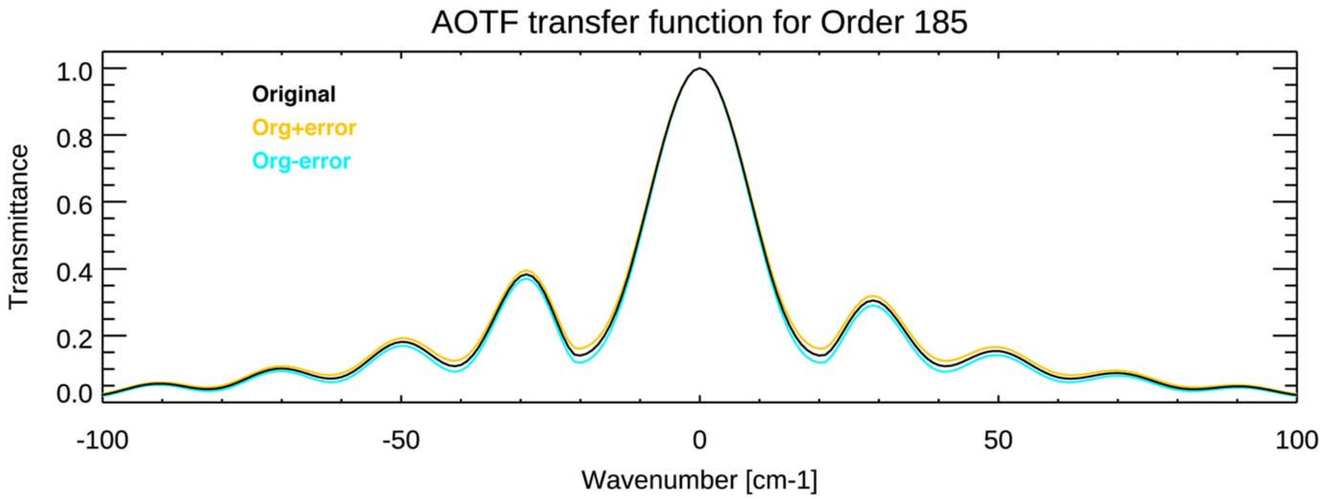

Figure A3. The AOTF transfer function for the order 185 of the NOMAD SO channel (the black curve). The orange and light blue curves show those shifted by one-sigma uncertainty in the Gaussian intensity parameter in the AOTF transfer function.

the retrievals. The evaluation of the uncertainty is performed by calculating the standard deviation in the fitting by second orders of the polynomial function to determine this parameter (see Figure FA1 in Villanueva et al. 2022). The red and blue curves in Figure A3 are the AOTF transfer function shifted by their uncertainty.

Appendix B
Vertical Profiles of Temperature Profile, CO Volume Mixing Ratios, and the Isotopic Ratios

In this appendix, vertical profiles of the temperature, volume mixing ratio of CO isotopes, and δ values are shown as Figure B1.

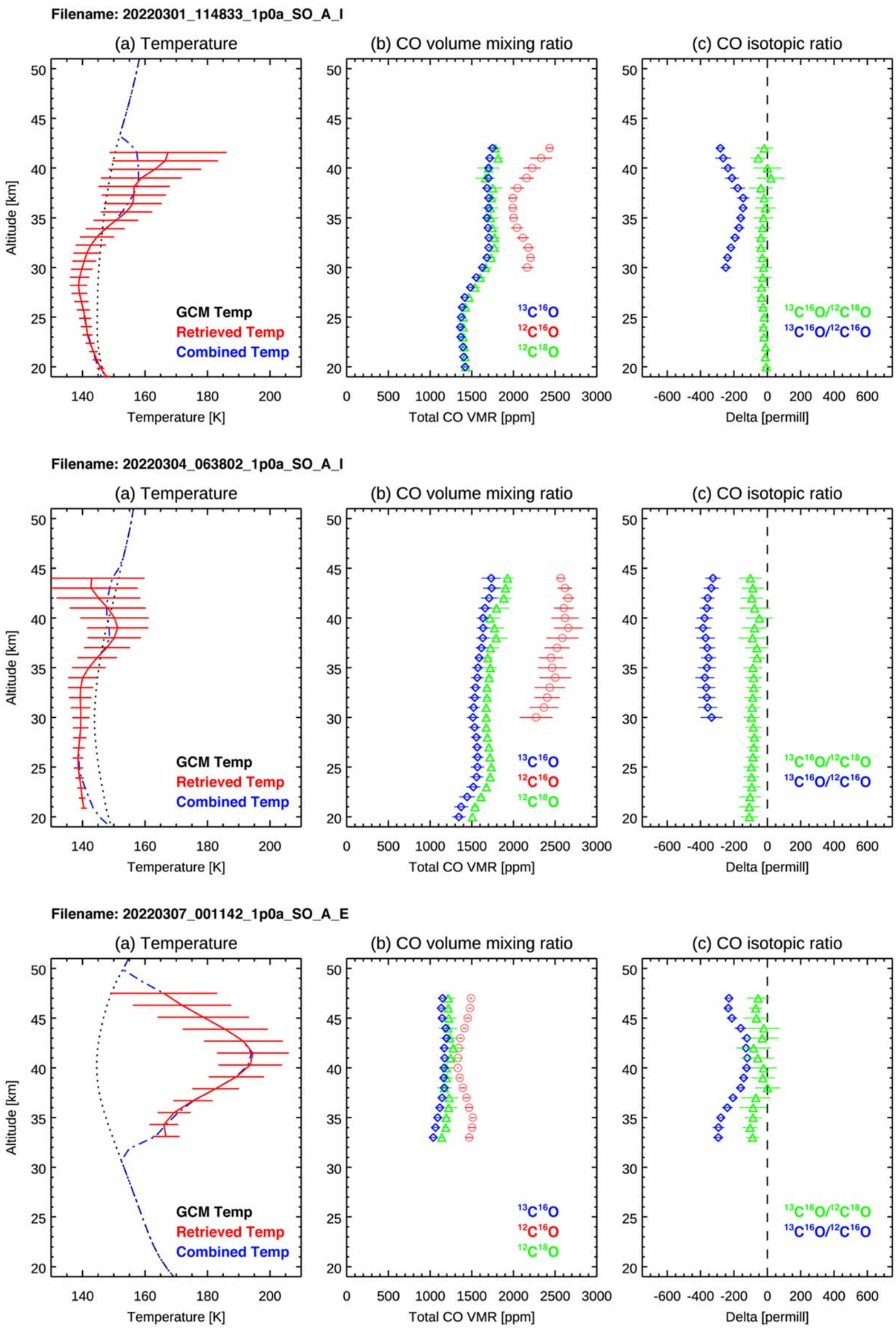

Figure B1. Same as Figure 4, but for the rest of the orbits.

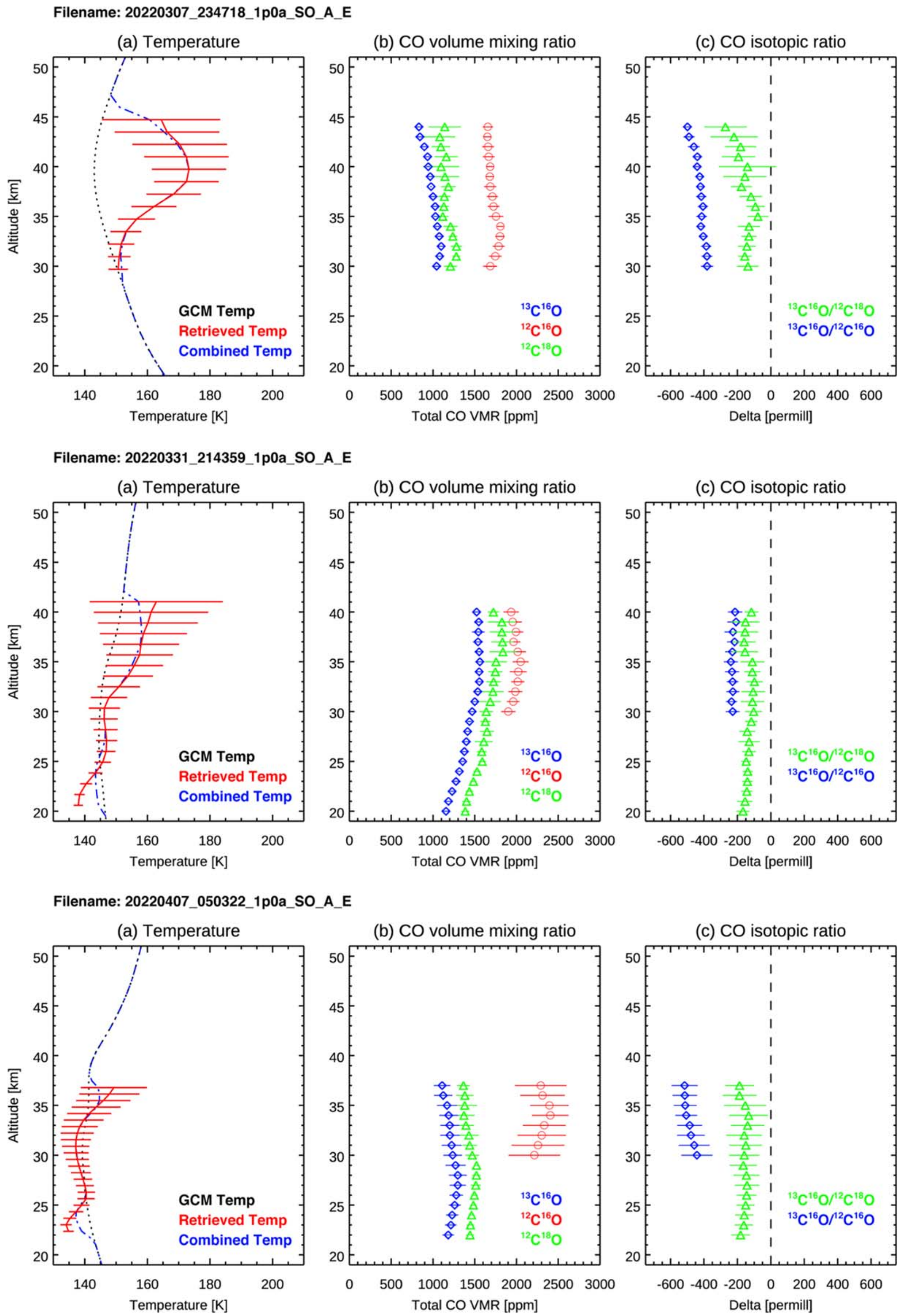

Figure B1. (Continued.)

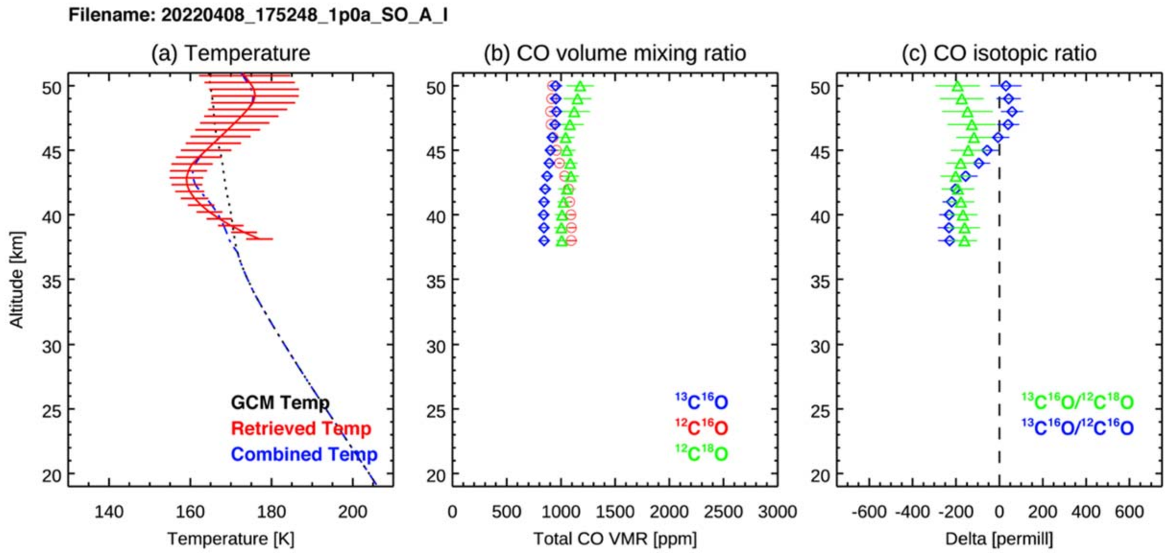

Figure B1. (Continued.)

ORCID iDs

S. Aoki https://orcid.org/0000-0001-6727-125X
N. Yoshida https://orcid.org/0000-0001-5214-5680
L. Trompet https://orcid.org/0000-0001-6259-2054
T. Yoshida https://orcid.org/0000-0001-5214-5680
N. Terada https://orcid.org/0000-0001-5685-9736
H. Nakagawa https://orcid.org/0000-0001-8166-0171
G. Liuzzi https://orcid.org/0000-0003-3638-5750
A. C. Vandaele https://orcid.org/0000-0001-8940-9301
I. R. Thomas https://orcid.org/0000-0003-3887-6668
G. L. Villanueva https://orcid.org/0000-0002-2662-5776
M. A. Lopez-Valverde https://orcid.org/0000-0002-7989-4267
A. Brines https://orcid.org/0000-0002-7044-3638
M. R. Patel https://orcid.org/0000-0002-8223-3566
S. Faggi https://orcid.org/0000-0003-0194-5615
F. Daerden https://orcid.org/0000-0001-7433-1839
J. T. Erwin https://orcid.org/0000-0003-0200-3195
B. Ristic https://orcid.org/0000-0002-9635-1125
G. Bellucci https://orcid.org/0000-0003-0867-8679
J. J. Lopez-Moreno https://orcid.org/0000-0002-7946-2624
H. Kurokawa https://orcid.org/0000-0003-1965-1586
Y. Ueno https://orcid.org/0000-0002-9095-4742

References

Alday, J., Trokhimovskiy, A., Irwin, P. G. J., et al. 2021a, NatAs, 5, 943
Alday, J., Wilson, C. F., Irwin, G. J., et al. 2019, A&A, 630, A91
Alday, J., Wilson, C. F., Irwin, P. G. J., et al. 2021b, JGRE, 126, e2021JE006992
Aoki, S., Daerden, F., Viscardy, S., et al. 2021, GeoRL, 48, e2021GL092506
Aoki, S., Vandaele, A. C., Daerden, F., et al. 2019, JGRE, 124, 3482
Aoki, S., Vandaele, A. C., Daerden, F., et al. 2022, JGRE, 127, e2022JE007231
Beale, C. A., Buzan, E. M., Boone, C. D., & Bernath, P. F. 2016, JMoSp, 323, 59
Clancy, R., & Muhleman, T. 1990, Icar, 85, 120
Daerden, F., Neary, L., Viscardy, S., et al. 2019, Icar, 326, 197
Gordon, I. E., Rothman, L. S., Hargreaves, R. J., et al. 2022, JQSRT, 277, 107949
Halevy, I., Fischer, W. W., & Eiler, J. M. 2011, PNAS, 108, 16895
House, G. H., Wong, G. M., Webster, C. R., et al. 2022, PNAS, 119, e2115651119
Korablev, O., Montmessin, F., Trokhimovskiy, A., et al. 2018, SSRv, 214, 7
Lammer, H., Scherf, M., Kurokawa, H., et al. 2020, SSRv, 216, 74
Lellouch, E., Gerin, M., Combes, F., Atreya, S., & Encrenaz, T. 1989, Icar, 77, 414
Lemoine, F. G., Smith, D. E., Rowlands, D. D., et al. 2001, JGR, 106, 23359
Liuzzi, G., Villanueva, G., Stone, S. W., et al. 2022, EPSC, 16, EPSC2022–575
Liuzzi, G., Villanueva, G. L., Viscardy, S., et al. 2021, GeoRL, 48, e2021GL092650
Niles, P. B., Leshin, L. A., & Guan, Y. 2005, GeCoA, 69, 2931
Schmidt, J. A., Johnson, M. S., & Schinke, R. 2013, PNAS, 110, 17691
Shaheen, R., Niles, P. B., Chong, K., Corrigan, C. M., & Thiemens, M. H. 2015, PNAS, 112, 336
Thiemens, M. 1999, Sci, 283, 341
Trokhimovskiy, A., Fedorova, A. A., Olsen, K. S., et al. 2021, A&A, 651, A32
Trompet, L., Vandaele, A. C., Thomas, I., et al. 2022a, JGRE, 128, e2022JE007277
Trompet, L., Vandaele, A. C., Thomas, I., et al. 2022b, JGRE, 128, e2022JE007279
Vandaele, A. C., Korablev, O., Daerden, F., et al. 2019, Natur, 568, 521
Vandaele, A. C., Kruglanski, M., & De Maziere, M. 2006, in Simulation and Retrieval of Atmospheric Spectra using ASIMUT, Atmospheric Science Conf. (Frascati: ESA)
Vandaele, A. C., Lopez-Moreno, J.-J., Patel, M. R., et al. 2018, SSRv, 214, 80
Villanueva, G., Liuzzi, L. G., Crisman, M. M. J., et al. 2021, SciA, 7, eabc8843
Villanueva, G. L., Liuzzi, G., Aoki, S., et al. 2022, GeoRL, 49, e2022GL098161
Webster, C. R., Mahaffy, P. R., Flesch, G. J., et al. 2013, Sci, 341, 260
Yoshida, T., Aoki, S., Ueno, Y., et al. 2023, PSJ, 4, 53